NEUROSCIENCE

Coupled electrophysiological, hemodynamic, and cerebrospinal fluid oscillations in human sleep

Nina E. Fultz[1,2], Giorgio Bonmassar[2,3], Kawin Setsompop[2,3], Robert A. Stickgold[4,5], Bruce R. Rosen[2,3], Jonathan R. Polimeni[2,3], Laura D. Lewis[1,2]*

Sleep is essential for both cognition and maintenance of healthy brain function. Slow waves in neural activity contribute to memory consolidation, whereas cerebrospinal fluid (CSF) clears metabolic waste products from the brain. Whether these two processes are related is not known. We used accelerated neuroimaging to measure physiological and neural dynamics in the human brain. We discovered a coherent pattern of oscillating electrophysiological, hemodynamic, and CSF dynamics that appears during non–rapid eye movement sleep. Neural slow waves are followed by hemodynamic oscillations, which in turn are coupled to CSF flow. These results demonstrate that the sleeping brain exhibits waves of CSF flow on a macroscopic scale, and these CSF dynamics are interlinked with neural and hemodynamic rhythms.

Sleep is crucial for both high-level cognitive processing and also basic maintenance and restoration of physiological function. During human non–rapid eye movement (NREM) sleep, the electroencephalogram (EEG) exhibits low-frequency (<4 Hz) oscillatory dynamics that support memory and neural computation (*1*–*8*). In addition, functional magnetic resonance imaging (fMRI) studies measuring blood oxygen level–dependent (BOLD) signals have demonstrated widespread hemodynamic alterations during NREM sleep (*9*–*15*). Sleep is also associated with increased interstitial fluid volume and clearance of metabolic waste products into the CSF (*16*), and clearance is stronger in sleep with more low-frequency EEG oscillations (*17*). Why these diverse physiological processes co-occur in this state of low arousal is not known. In particular, it remains unclear how CSF dynamics change during sleep and how they relate to the major changes in neural activity and hemodynamics.

We simultaneously measured BOLD fMRI dynamics, EEG, and CSF flow during human sleep. To achieve high–temporal-resolution imaging, we acquired fMRI data at fast rates [repetition time (TR) < 400 ms]. While fMRI is often used to detect local oxygenation changes, fast acquisition paradigms also enable detection of fluid inflow: Fresh fluid arriving at the edge of the imaging volume has high signal intensity because it has not yet experienced radiofrequency pulses (fig. S1). By placing the boundary edge of the imaging volume at the fourth ventricle (Fig. 1A), CSF flow into the brain was detected as increased signal in the lower slices (Fig. 1B), allowing us to measure dynamics of CSF flow simultaneously with BOLD fMRI. We combined this imaging with simultaneous EEG (n = 13 participants) and identified continuous segments of clear stable wake or NREM sleep with low motion (fig. S2 and materials and methods) to enable analysis of continuous low-frequency dynamics.

We first investigated whether sleep was associated with distinct CSF flow dynamics (Fig. 1, C to E). During wakefulness, the CSF signal exhibited a small-amplitude rhythm synchronized to the respiratory signal at ~0.25 Hz (Fig. 1, E and G), consistent with previous studies (*18*, *19*). By contrast, during NREM sleep, we observed a large oscillation in the CSF signal at 0.05 Hz (Fig. 1, E and G). We analyzed this CSF signal across all sleep segments, confirming that identified sleep segments exhibited low-frequency EEG signatures of NREM sleep (Fig. 1F). We found a 5.52-dB increase in the CSF signal peaking at 0.05 Hz during sleep (Fig. 1, G and H, and fig. S2) [95% confidence interval (CI) = (2.33, 7.67); P = 0.003, signed-rank test], suggesting that large waves of CSF inflow occur approximately every 20 s. We additionally analyzed nearby non-CSF regions of interest (ROIs) with matched slice positioning and saw no such effect [change = −0.03 dB, CI = (−2.7, 1.3); P = 0.003 for difference, signed-rank test], suggesting that this sleep-associated pattern was specifically driven by physiological signals in the ventricle (Fig. 1I).

Because inflow signals are caused by fluid flowing into the acquisition volume, CSF flow signals should be brightest in edge slices and decay as fluid passes into central slices (Fig. 2, A and B, and fig. S1). We indeed observed a gradient of signal amplitudes across the slices (Fig. 2, C and D). Some large inflow events exhibited equally bright amplitudes across the lower slices (Fig. 2D), suggesting the CSF flow velocity had exceeded the imaging critical velocity (11.4 mm/s for slice 2). Together, these results identified a large-amplitude pulsatile flow of CSF at 0.05 Hz that appears during NREM sleep.

We next examined whether these slow macroscopic CSF oscillations were linked to hemodynamic signals. Previous studies have proposed microscopic arterial pulsation, corresponding to the ~1-Hz cardiac cycle, as a mechanism for driving interstitial fluid flow (*20*–*23*). To test what might generate the much slower macroscopic CSF rhythm we observed, we analyzed the changes in BOLD signal during sleep. We observed an increase in BOLD signal amplitude in the cortical gray-matter fMRI signal during sleep, as compared with wakefulness (Fig. 3A versus B and C) [mean = 3.28 dB; CI = (0.09, 6.54); P = 0.032, signed-rank test], consistent with previous reports of low-frequency BOLD fluctuations during sleep (*9*, *10*, *24*). Furthermore, the CSF signal was tightly temporally coupled to the cortical gray-matter BOLD oscillation during sleep (Fig. 3, A and B), exhibiting a strong anticorrelation (fig. S3) (maximal r = −0.48 at lag 2 s, P < 0.001, shuffling).

This anticorrelation suggested a possible alternation of blood flow and CSF flow during sleep. We hypothesized that the BOLD oscillations corresponded to an oscillation in cerebral blood volume and that, because of constant intracranial volume, more CSF flows into the head when less volume is occupied by the blood (*25*, *26*). This hypothesis predicts that the CSF signal should approximately match the negative derivative of the BOLD oscillation, after setting negative values to zero (materials and methods). Consistent with this hypothesis, the CSF time series and the thresholded derivative BOLD signals were strongly correlated (Fig. 3, D and E) (maximal r = 0.59 at lag −1.8 s; P < 0.001, shuffling).

We next examined whether neural activity was linked to these coupled hemodynamic and CSF oscillations during sleep. In conventional fMRI, the BOLD response is elicited by neural activity, which drives flow of oxygen-rich blood (*27*, *28*), and EEG oscillations are associated with hemodynamic signals (*29*–*32*). We therefore hypothesized that the large, slow-delta (0.2 to 4 Hz) electrophysiologic oscillations characteristic of NREM sleep could be coupled to oscillations in blood volume and, in turn, displacement effects on CSF flow. We analyzed the instantaneous amplitude of slow-delta EEG relative to the peak of the CSF waves and found that neural, BOLD, and CSF waves were coupled (Fig. 4, A to C, and fig. S4). The neural waves preceded the CSF waves, with a peak in slow-delta EEG occurring 6.4 s before the CSF peak (peak amplitude = 21%, P < 0.001, shuffling). We calculated the best-fit impulse response between the EEG and CSF (Fig. 4D)

[1]Department of Biomedical Engineering, Boston University, Boston, MA 02215, USA. [2]Athinoula A. Martinos Center for Biomedical Imaging, Massachusetts General Hospital, Boston, MA 02129, USA. [3]Department of Radiology, Harvard Medical School, Boston, MA 02115, USA. [4]Department of Psychiatry, Beth Israel Deaconess Medical Center, Boston, MA 02215, USA. [5]Department of Psychiatry, Harvard Medical School, Boston, MA 02115, USA.
*Corresponding author. Email: ldlewis@bu.edu

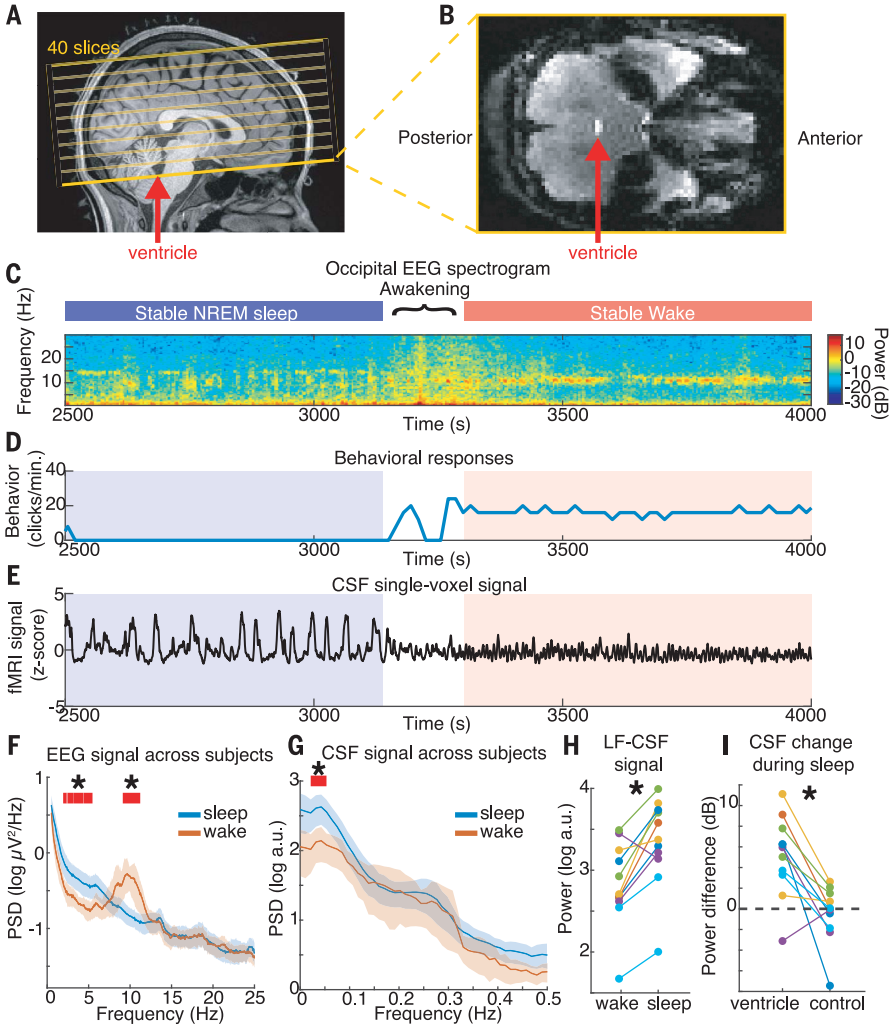

Fig. 1. Large oscillations in CSF signals appear in the fourth ventricle during sleep. (**A**) Example scan positioning. Thick yellow line: position of the functional image relative to the anatomy. The bottom edge intersects with the fourth ventricle (red arrow), allowing CSF inflow to be measured. A subset of the 40 acquired slices are displayed. (**B**) Example functional image from the bottom slice. Inflow through the ventricle is detected as a bright signal (red arrow). (**C**) EEG spectrogram from this individual shows long periods of NREM sleep and wake (~10 Hz occipital alpha). (**D**) Behavioral responses from this individual. (**E**) Time series of a single CSF voxel (smoothed with 10-TR kernel) shows large, slow dynamics in sleep that subside during wakefulness. (**F**) Mean power spectral density (PSD) of occipital EEG confirms slow-delta power in sleep, as opposed to high alpha power in wake (n = 13 participants sleep; 11 participants wake). (**G**) PSD of CSF signal shows increased 0.05 Hz power during sleep (n = 13 participants sleep; 11 participants wake). Shaded regions denote 95% CIs; red lines and asterisks mark non-overlapping CIs. (**H**) Low-frequency (LF, 0 to 0.1 Hz) CSF power increased during sleep (n = 11 participants for pairwise comparison). a.u., arbitrary units. (**I**) This sleep-selective power increase was specific to the ventricle ROI and not observed in a neighboring size-matched control ROI (n = 11 participants).

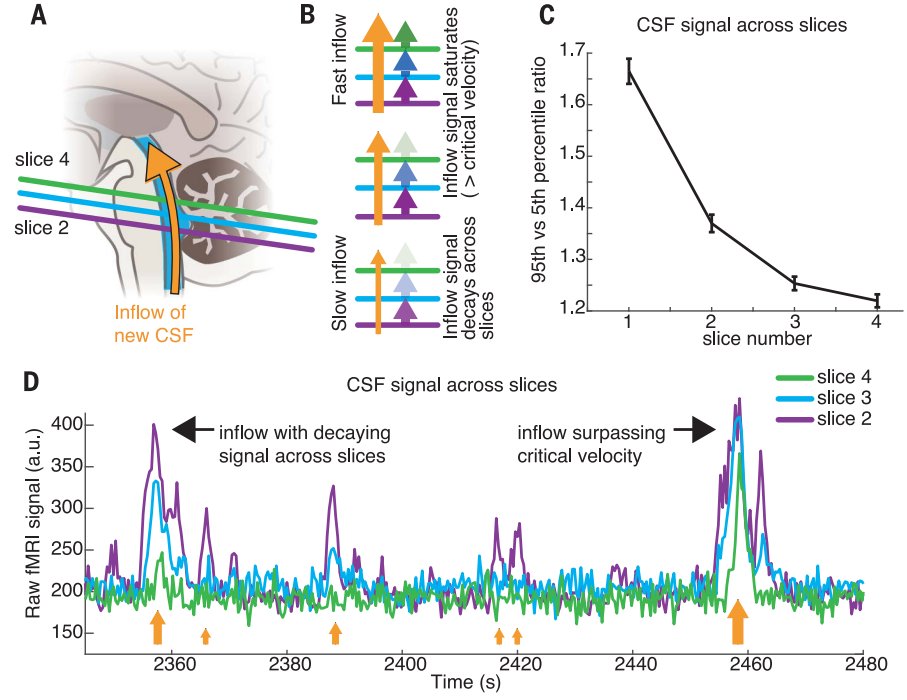

Fig. 2. Ventricle signals correspond to a ~0.05-Hz pulsatile inflow of CSF. (**A**) Schematic of acquisition. New CSF flowing into the imaging volume will generate bright signals. (**B**) Inflow signals will be largest in the bottom slice and decrease in amplitude inwards. If flow exceeds the critical velocity, then CSF in the bottom slice is completely replaced, and signal amplitudes are large in inner slices as well. (**C**) Mean amplitude across slices decays in ascending slices. Error bars are standard error across all sleep segments, with the ROI present in four contiguous slices (n = 129 segments, 11 participants). (**D**) Example time series from the bottom slices of the imaging volume in the fourth ventricle demonstrates the largest signal in the lower slices (e.g., second) and smaller signals in higher slices (e.g., fourth). Orange arrows schematically illustrate flow velocity (larger arrows denote higher velocity), and black arrows point out individual events.

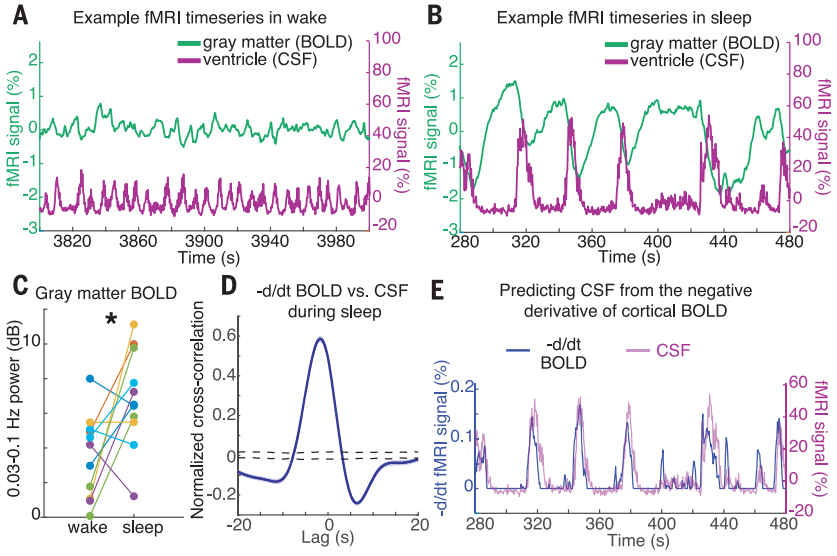

Fig. 3. CSF flow oscillations are anticorrelated to a hemodynamic oscillation in the cortical gray matter that appears during sleep, with CSF flow increasing when blood volume decreases. (**A**) Example time series of the cortical gray-matter BOLD signal and the mean CSF signal from one participant. During wake, signals are low-amplitude and synchronized to respiration (0.25 Hz). (**B**) During sleep, a large-amplitude BOLD oscillation appears, and its time course is coupled to the ventricle CSF signal (~0.05 Hz). (**C**) Mean cortical gray-matter BOLD signal power increases during sleep (n = 11 participants for pairwise test). (**D**) Mean cross-correlation between the zero-thresholded negative derivative of BOLD and CSF signals shows strong correlation (n = 176 segments, 13 participants). The shaded blue region indicates the standard error across segments; the black dashed line denotes the 95% interval of shuffled distribution. (**E**) Example time series showing the correlation, suggesting that CSF flows up the fourth ventricle when cerebral blood volume decreases.

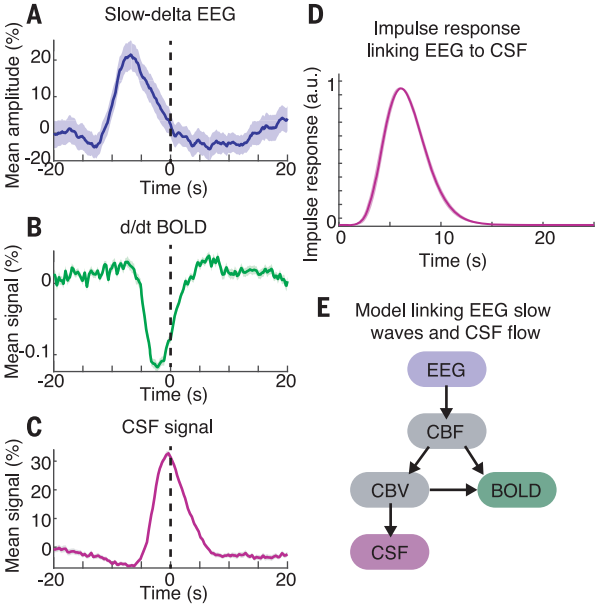

Fig. 4. EEG slow-delta waves are coupled to and precede BOLD and CSF oscillations. (**A**) Mean amplitude envelope of slow-delta EEG, (**B**) mean derivative of BOLD signals, and (**C**) mean CSF signal, all locked to the peaks of CSF waves during sleep. The shaded region represents the standard error across peak-locked trials (n = 123 peaks). (**D**) Calculated impulse response of the CSF signal to the EEG envelope shows a time course similar to that of previously established hemodynamic models. Shading indicates standard deviation across model folds. (**E**) Diagram of model linking the time course of neural activity to CSF flow. Variables include CBF and cerebral blood volume (CBV).

and found that convolving the EEG with this impulse response yielded a significant prediction of CSF dynamics (fig. S5A) (zero-lag r = 0.23, cross-validated r = 0.22 ± 0.07). To examine whether this EEG-CSF coupling was specifically linked to the appearance of CSF waves during sleep, we tested how well the EEG predicted CSF dynamics in the segments with the largest CSF waves. Performance was higher in segments with larger CSF waves (fig. S5, B and C) (zero-lag r = 0.54, P < 0.001, shuffling), suggesting that the EEG was more strongly linked to CSF in the sleep segments richest in CSF waves.

The coherent dynamics of the EEG, BOLD, and CSF signals thus exhibited a specific timing sequence, with neural rhythms preceding subsequent BOLD and CSF waves. To test whether these observed correlations and delay patterns could arise from biophysical mechanisms, we constructed a computational model using established models of hemodynamic coupling (Fig. 4E and fig. S6). We extracted the envelope of slow-delta EEG, expected to correlate with decreases in cerebral blood flow (CBF) signal because of its associated suppression of neural activity (*2*). The neural oscillation was then used to predict the time courses of blood flow, blood volume, and CSF (*33*, *34*). The model first used previously reported physiological parameters (*35*), with no additional parameter fitting, to test whether our observations were consistent with established biophysical coupling between these signals. This model performed as well as the best-fit impulse response [zero-lag R = 0.22; CI across segments = (0.16, 0.27); P < 0.001, shuffling] (fig. S6 and S7). The model prediction was significantly larger than the maximal correlation between the original EEG envelope and CSF across all lags (maximal r = 0.15, P < 0.05), demonstrating that our data were consistent with biophysical coupling between neural activity, hemodynamics, and CSF.

We conclude that human sleep is associated with large coupled low-frequency oscillations in neuronal activity, blood oxygenation, and CSF flow. Although electrophysiological slow waves are known to play important roles in cognition (*1*), our results suggest that they may also be linked to the physiologically restorative effects of sleep, as slow neural activity is followed by brain-wide pulsations in blood volume and CSF flow.

These results address a key missing link in the neurophysiology of sleep. The macroscopic changes in CSF flow that we identified are expected to alter waste clearance, as pulsatile fluid dynamics can increase mixing and diffusion (*20*, *21*, *36*). Neurovascular coupling has been proposed to contribute to clearance (*37*), but why it would cause higher clearance rates during sleep was not known. Our study suggests slow neural and hemodynamic oscillations

as a possible contributor to this process, in concert with other physiological factors. Studies in animals could next test for causal relationships between these neural and physiological rhythms.

Our identification of sleep-associated CSF fluid dynamics also suggests a potential biomarker to be explored in clinical conditions associated with sleep disturbance. Memory impairment in aging is associated with suppressed slow waves (*38*); our model suggests that this slow-wave loss would, in turn, be associated with decreased CSF flow. Furthermore, our results hint at a potential bridge between recent findings that tau CSF levels and amyloid beta depend on sleep and neural activity (*39*–*41*) and that oscillatory neural activity leads to reduced tau (*42*)—coherent neural activity might signal higher protein aggregate clearance. Taken together, our results identify waves of CSF flow that appear during sleep and show that slow rhythms in neural activity are interlinked with these CSF waves, with hemodynamic oscillations as an intermediate mechanism through which these processes are coupled.

REFERENCES AND NOTES

1. S. Diekelmann, J. Born, *Nat. Rev. Neurosci.* **11**, 114–126 (2010).
2. M. Steriade, A. Nuñez, F. Amzica, *J. Neurosci.* **13**, 3252–3265 (1993).
3. M. Massimini, R. Huber, F. Ferrarelli, S. Hill, G. Tononi, *J. Neurosci.* **24**, 6862–6870 (2004).
4. L. Marshall, H. Helgadóttir, M. Mölle, J. Born, *Nature* **444**, 610–613 (2006).
5. A. Destexhe, D. Contreras, in *Sleep and Anesthesia*, A. Hutt, Ed. (Springer, 2011), p. 258.
6. E. J. W. Van Someren, Y. D. Van Der Werf, P. R. Roelfsema, H. D. Mansvelder, F. H. L. da Silva, *Prog. Brain Res.* **193**, 3–15 (2011).
7. V. V. Vyazovskiy, K. D. Harris, *Nat. Rev. Neurosci.* **14**, 443–451 (2013).
8. B. O. Watson, D. Levenstein, J. P. Greene, J. N. Gelinas, G. Buzsáki, *Neuron* **90**, 839–852 (2016).
9. M. Fukunaga *et al*., *Magn. Reson. Imaging* **24**, 979–992 (2006).
10. S. G. Horovitz *et al*., *Hum. Brain Mapp.* **29**, 671–682 (2008).
11. A. Mitra, A. Z. Snyder, E. Tagliazucchi, H. Laufs, M. E. Raichle, *eLife* **4**, e10781 (2015).
12. M. Boly *et al*., *Proc. Natl. Acad. Sci. U.S.A.* **109**, 5856–5861 (2012).
13. T. T. Dang-Vu *et al*., *Proc. Natl. Acad. Sci. U.S.A.* **105**, 15160–15165 (2008).
14. C. Kaufmann *et al*., *Brain* **129**, 655–667 (2006).
15. L. J. Larson-Prior *et al*., *Proc. Natl. Acad. Sci. U.S.A.* **106**, 4489–4494 (2009).
16. L. Xie *et al*., *Science* **342**, 373–377 (2013).
17. L. M. Hablitz *et al*., *Sci. Adv.* **5**, eaav5447 (2019).
18. S. Dreha-Kulaczewski *et al*., *J. Neurosci.* **35**, 2485–2491 (2015).
19. V. Kiviniemi *et al*., *J. Cereb. Blood Flow Metab.* **36**, 1033–1045 (2016).
20. D. Schley, R. Carare-Nnadi, C. P. Please, V. H. Perry, R. O. Weller, *J. Theor. Biol.* **238**, 962–974 (2006).
21. J. J. Iliff *et al*., *J. Neurosci.* **33**, 18190–18199 (2013).
22. H. Mestre *et al*., *Nat. Commun.* **9**, 4878 (2018).
23. I. F. Harrison *et al*., *eLife* **7**, e34028 (2018).
24. P. S. Özbay *et al*., *Neuroimage* **176**, 541–549 (2018).
25. A. Scouten, R. T. Constable, *Magn. Reson. Med.* **59**, 308–315 (2008).
26. S. K. Piechnik, J. Evans, L. H. Bary, R. G. Wise, P. Jezzard, *Magn. Reson. Med.* **61**, 579–586 (2009).
27. S. Ogawa, T. M. Lee, A. R. Kay, D. W. Tank, *Proc. Natl. Acad. Sci. U.S.A.* **87**, 9868–9872 (1990).
28. K. K. Kwong *et al*., *Proc. Natl. Acad. Sci. U.S.A.* **89**, 5675–5679 (1992).
29. N. K. Logothetis, J. Pauls, M. Augath, T. Trinath, A. Oeltermann, *Nature* **412**, 150–157 (2001).
30. B. J. He, M. E. Raichle, *Trends Cogn. Sci.* **13**, 302–309 (2009).
31. C. Mateo, P. M. Knutsen, P. S. Tsai, A. Y. Shih, D. Kleinfeld, *Neuron* **96**, 936–948.e3 (2017).
32. M. L. Schölvinck, A. Maier, F. Q. Ye, J. H. Duyn, D. A. Leopold, *Proc. Natl. Acad. Sci. U.S.A.* **107**, 10238–10243 (2010).
33. R. B. Buxton, K. Uludağ, D. J. Dubowitz, T. T. Liu, *Neuroimage* **23** (suppl. 1), S220–S233 (2004).
34. K. J. Friston, A. Mechelli, R. Turner, C. J. Price, *Neuroimage* **12**, 466–477 (2000).
35. A. B. Simon, R. B. Buxton, *Neuroimage* **116**, 158–167 (2015).
36. M. Asgari, D. de Zélicourt, V. Kurtcuoglu, *Sci. Rep.* **6**, 38635 (2016).
37. A. K. Diem, R. O. Carare, R. O. Weller, N. W. Bressloff, *PLOS ONE* **13**, e0205276 (2018).
38. B. A. Mander *et al*., *Nat. Neurosci.* **16**, 357–364 (2013).
39. J. K. Holth *et al*., *Science* **363**, 880–884 (2019).
40. E. Shokri-Kojori *et al*., *Proc. Natl. Acad. Sci. U.S.A.* **115**, 4483–4488 (2018).
41. J.-E. Kang *et al*., *Science* **326**, 1005–1007 (2009).
42. H. F. Iaccarino *et al*., *Nature* **540**, 230–235 (2016).
43. N. E Fultz *et al*., Sleep-wake imaging ROI time series. Figshare (2019); doi: 10.6084/m9.figshare.9992054.

ACKNOWLEDGMENTS

We thank T. Witzel for contributing to the imaging, J. Voigts and C. Robertson for comments, and S. Williams, K. Gupta, and M. Albrecht for assistance. **Funding:** This work was supported by the National Institutes of Health (R00-MH111748, R01-EB019437, P41-EB015896, R01-MH111419, R01-MH048832, R01-EB024343, R01-MH111438, R21-NS106706, S10-RR023043, and S10-OD010759) and the Martinos Center for Biomedical Imaging. **Author contributions:** All authors contributed to experiment design; L.D.L. and N.E.F. collected and analyzed data; L.D.L. wrote the manuscript; and all authors edited the manuscript. **Competing interests:** L.D.L., B.R.R., and J.R.P. are inventors on a provisional patent coversheet. **Data availability:** The ROI and EEG time series reported here are available at Figshare (*43*).

SUPPLEMENTARY MATERIALS

science.sciencemag.org/content/366/6465/628/suppl/DC1
Materials and Methods
Supplementary Text
Figs. S1 to S10
References (*44*–*57*)

View/request a protocol for this paper from *Bio-protocol*.

15 April 2019; accepted 18 September 2019
10.1126/science.aax5440